Investigation of time-of-flight benefits in an LYSO-based PET/CT scanner: A Monte Carlo study using GATE

P. Geramifar [a,b,c], M.R. Ay [b,c,d,*], M. Shamsaie Zafarghandi [a], S. Sarkar [b,c], G. Loudos [e], A. Rahmim [f,g]

[a] Faculty of Physics and Nuclear Engineering, Amir Kabir University of Technology (Tehran Polytechnic), Tehran, Iran
[b] Research Center for Science and Technology in Medicine, Tehran University of Medical Sciences, Tehran, Iran
[c] Research Institute for Nuclear Medicine, Tehran University of Medical Sciences, Shariati Hospital, Tehran, Iran
[d] Department of Medical Physics and Biomedical Engineering, Tehran University of Medical Sciences, Tehran, Iran
[e] Department of Medical Instruments Technology, Technological Educational Institute, Athens, Greece
[f] Department of Radiology, School of Medicine, Johns Hopkins University, Baltimore, USA
[g] Department of Electrical and Computer Engineering, School of Engineering, Johns Hopkins University, Baltimore, USA

ARTICLE INFO

ABSTRACT

The advent of fast scintillators yielding great light yield and/or stopping power, along with advances in photomultiplier tubes and electronics, have rekindled interest in time-of-flight (TOF) PET. Because the potential performance improvements offered by TOF PET are substantial, efforts to improve PET timing should prove very fruitful. In this study, we performed Monte Carlo simulations to explore what gains in PET performance could be achieved if the coincidence resolving time (CRT) in the LYSO-based PET component of Discovery RX PET/CT scanner were improved. For this purpose, the GATE Monte Carlo package was utilized, providing the ability to model and characterize various physical phenomena in PET imaging. For the present investigation, count rate performance and signal to noise ratio (SNR) values in different activity concentrations were simulated for different coincidence timing windows of 4, 5.85, 6, 6.5, 8, 10 and 12 ns and with different CRTs of 100–900 ps FWHM involving 50 ps FWHM increments using the NEMA scatter phantom. Strong evidence supporting robustness of the simulations was found as observed in the good agreement between measured and simulated data for the cases of estimating axial sensitivity, axial and transaxial detection position, gamma non-collinearity angle distribution and positron annihilation distance. In the non-TOF context, the results show that the random event rate can be reduced by using narrower coincidence timing window widths, demonstrating considerable enhancements in the peak noise equivalent count rate (NECR) performance. The peak NECR had increased by ∼50% when utilizing the coincidence window width of 4 ns. At the same time, utilization of TOF information resulted in improved NECR and SNR with the dramatic reduction of random coincidences as a function of CRT. For example, with CRT of 500 ps FWHM, a factor of 2.3 reduction in random rates, factor of 1.5 increase in NECR and factor of 2.1 improvement in SNR is achievable. The results of this study show that in addition to the high sensitivity of Discovery RX PET/CT scanner, the implementation of TOF with proper CRT can efficiently improve the image quality in this scanner. Having successfully simulated the DRX scanner and utilization of TOF information, our research goal is to use the Monte Carlo simulation technique to arrive at powerful, accurate and feasible reconstruction algorithms.

1. Introduction

Positron Emission Tomography is a functional medical imaging modality that utilizes coincidence detection of collinear annihilation photons to reconstruct a quantitative image of the in vivo radio-tracer distribution. Like most imaging modalities, PET is limited by statistical noise. By accurately measuring the arrival time of the two 511 keV positron annihilation photons in the ring of detectors that surrounds the patient, the location at which the positron has annihilated can be constrained. This technique is known as time-of-flight (TOF) PET [1]. Straightforward theoretical considerations predict that the statistical noise variance in PET images can be reduced by using TOF information [2,3]. This reduction can be obtained by improving the CRT, and so would be achievable in clinical, whole-body studies using PET systems that differ little from existing cameras. TOF PET was first studied in the 1980s [4–6], but gradually faded away, as it was not possible at the time to achieve

* Corresponding author at: Department of Medical Physics and Biomedical Engineering, Tehran University of Medical Sciences, Tehran, Iran.
Tel./fax: +0098 21 66466383.
E-mail address: mohammadreza_ay@tums.ac.ir (M.R. Ay).

sufficient CRT without sacrificing other important PET performance aspects, such as spatial resolution and efficiency. With the advent of fast scintillators with greater light yield and/or stopping power, along with advances in photomultiplier tubes and electronics, interest in TOF PET has been rekindled [2].

The key advance that prompted re-evaluation of TOF PET was the development of new scintillator materials. One such material amongst the cerium-doped oxyorthosilicate PET scintillators, which is very prevalently utilized nowadays in PET scanners, is lutetium yttrium orthosilicate (LYSOl). This scintillator possesses excellent characteristics for detecting 511-keV photons in PET: The effective atomic number is 65; the density is 7.1 g/cm3, and the attenuation coefficient is 0.83 cm^{-1} at 511 keV; the scintillation decay time is 42 ns and it has a light yield that is similar to that of LSO [7]. It should be mentioned that the values of these properties depend on the relative yttrium content.

There have been several studies investigating the benefits of TOF for clinical PET [8–12]. A clear correlation between patient body mass index and gain in SNR was observed with a gain due to TOF ranging from 1.1 to 1.8, which is consistent with the 590-ps time resolution of the TOF PET scanner [8]. TOF PET provides a significant improvement in observer performance for detecting focal warm lesions in a noisy background and staging disease for various patient sizes and count levels [9]. This implies that TOF can be beneficial in situations where few counts are collected, e.g., dynamic imaging, respiratory gating and imaging with non-pure positron emitters. Utilization of the TOF information may result in improved image quality in most of the parameters used for the assessment, particularly resolution of image detail, definition of small lesions and image uniformity [9–11]. It is important to note that incorporating TOF information within the reconstruction will especially benefit heavy patients [12]. TOF PET scanners can now be designed to have all the desirable features and high performance of non-TOF scanners with the added benefits of the TOF image improvements [13].

The aim of this study was to predict what gains in PET performance could be achieved if the CRT in the LYSO-based PET component of Discovery RX PET/CT scanner [14] were improved. In TOF performance evaluation, we clearly show that the commonly used equation for estimating SNR gain due to TOF is not a realistic approximation since it is assumed that the variance contributions due to true, scatter and random coincidences decrease by the same factor and that NECR terms for TOF and conventional images are the same. Although NECR is a raw data quality metric that does not take into account the impact of reconstruction algorithms on image quality, but as being directly proportional to the square of the signal to noise ratio of the acquired data in both 2-D and 3-D acquisition modes, as well as for the different activity distributions, it has been used as a surrogate metric for image quality over the last 2 decades [15–20].

For this purpose, a GATE Monte Carlo model for the simulation of the scanner was validated and an accurate model for further research regarding the time of flight benefits was achieved [21]. The assessment was conducted by Monte Carlo simulations after accurate validation of the simulations through comparisons with measured data.

2. Methods and materials

2.1. Monte Carlo simulation

Full scanner simulation is based on the GATE (Geant4 Application for Tomographic Emission) toolkit which is developed and maintained by the Open-GATE collaboration [22]. The GATE Monte Carlo package is designed to simulate PET and SPECT systems and define all the simulation parameters including complex detector, phantom and source distribution geometry modeling (e.g. [23–28]).GATE uses combinations of simple shapes (e.g., boxes, spheres and cylinders), as defined in GEANT4 to generate complex geometric structures [29]. The software's limitations with regard to generating adequately complex shapes are well within the tolerance and design of these scanners [21]. GATE has the ability to convert photon interactions into counts in a manner analogous to that of a real scanner's detectors and electronics. This is accomplished in GATE by a series of signal processing chains, namely the digitizer. Several functions are grouped in the digitizer to simulate the behavior of the scanner's detectors (i.e. build physical observables from the hits, model readout schemes and trigger logics), each of them is represented by a module. Each module of the digitizer mimics a separate portion of a real scanner behavior. The crystal quantum efficiency (QE), crystal blurring, thresholder, upholder, deadtime and other electronics delay are defined in this module. To mimics the effect of limited transfer rate, a module allows to simulate the data loss due to an overflow of a memory buffer, limited bandwidth of wires or buffer capacities of the I/O interfaces.

We should stress here that as we did not access to detailed information of electronic system of DRX, so we estimated those values by choosing the ones that minimized the relative difference in the simulated and measured sensitivity. Furthermore, the phenomena within a real detector-signal processing chain including block non-uniform energy resolutions, light spread and leakage, PMT and optical coupling efficiencies and finally the patient bed were not modeled in the simulation.

2.2. Discovery RX PET/CT scanner

The Discovery RX (GE Healthcare Technologies, Waukesha, WI, USA) PET/CT scanner [14] uses LYSO scintillators. It uses $4.2 \times 6.3 \times 30$ mm^3 LYSO crystals grouped in 9×6 blocks. There are 24 rings with 630 crystals per ring for a grand total of 15,120 crystals and the ring diameter is 88.6 cm. The transaxial and axial fields of view are 70 and 15.7 cm, respectively. The scanner has retractable septa and can operate in both 2-dimensional (2D) and 3-dimensional (3D) modes. The coincident window width is 5.85 ns and the energy window is 425–650 keV. The canner has transaxial resolution of 4.8 mm at 1 cm in both 2D and 3D mode.

2.3. Model description

In this section the simulated model (geometry and signal processing) are described in detail.

2.3.1. Geometry

In accordance with the real scanner, our three-dimensional PET simulation model of the scanner consists of 15,120 detectors grouped into blocks, which are grouped into modules. The scanner has 35 detector modules arranged in a ring. Each of these modules is comprised of eight detector blocks which in turn contain 54 crystals each. This arrangement consists of 24 detection rings, each one with 630 crystals, for a grand total of 15,120 crystals.

The dimensions of the individual crystals were 4.2 mm transaxial, 6.3 mm axial and 30 mm radial. The shielding and packing materials within the detector blocks and the shielding surrounding the scanner rings are also accounted for in the model. The phantoms are modeled separately using the dimensions and tolerances as described in the published NEMA standards [30].

2.3.2. Signal processing

The data collection system within GATE enables the modeling of the signal processing chain that is analogous to that of a real PET scanner. GATE also has the ability to convert photon interactions into counts in a manner analogous to that of a real scanner's detectors and electronics. This is accomplished in GATE by a series of signal processing routines known collectively as the *digitizer*. A sequence of digitizer modules to simulate the complete signal processing chain was used in the simulation (Fig. 1).

This sequence began with the *Adder* module which integrates the energy deposition of a particle interacting within a single crystal.

Next, the Readout module integrates the results from the Adder module within a block of crystals to create a pulse. Then a *Blurring* module applies a detection efficiency factor. Next, a *Deadtime* module is inserted to create deadtime at the Block level that is triggered by the pulses within a block. Following this, another deadtime module is applied at the Module level of the scanner to account for the multiplexor processing of the single events. An energy-window discriminator is then applied via the *Thresholder* and *Upholder* modules. Finally, the remaining pulses are sorted by the *Coincidence* module.

2.4. Simulation setup

As specified by NEMA, six concentric aluminum tubes all 700 mm in length were used to detect camera sensitivity. A line source with 16 MBq of 18 F was placed in the innermost tube, a fillable polyethylene tube with inside diameter of 1 mm and outside diameter of 3 mm. The scatter fraction (SF) and counting rate measurements were performed using the NEMA scatter phantom (the 70 cm in length cylindrical tube with outside diameter of 20.3 cm and a 6.4 mm hole size at offset distance of 4.5 cm). The 80 cm line source is placed in the hole with different activity of 220 MBq–1 GBq. In all the simulations the acquisition time of 10 s was selected. After accurate modeling of the scanner's geometry into the code the simulation setup were as follows.

A 14% mean energy resolution was applied to all crystals at the energy reference of 511 keV. Also two non paralyzable dead times, a 150 ns deadtime for the singles at the Block level followed by a 75 ns deadtime for the coincidence count rate were used. Once the coincidences were formed, some treatment should be applied on to reproduce sources of count loss that may occur because of the acquisition limitations. Thus, a memory buffer of 32 coincidences, in an event by event basis was applied. The mentioned buffer satisfactorily matches the count rates in experimental results at higher activities. In order to explore what gains in PET performance could be achieved if the CRT were improved, count rate performance, NECR curves and SNR values were obtained in different activity concentrations for varying coincidence timing windows of 4, 5.85, 6, 6.5, 8, 10 and 12 ns and with different CRTs of 100–900 ps FWHM with 50 ps FWHM increments using the NEMA scatter phantom. It should be mentioned the lower limit of 100 ps FWHM, has recently been demonstrated in a lab-scale setup using the new scintillator LaBr3:Ce and a few

Fig. 1. Signal processing chain simulated by GATE used to convert the particle interactions into coincidence counts.

recent publications on new scintillators, light sensors and timing methods provide some hope that the studied CRTs could actually be achieved in a realistic PET system [31–34].

The code was validated via comparison with measured data for NEMA measurements [30] of the Discovery RX scanner published by Kemp et al. [14].

2.5. TOF performance evaluation

Brownell [35] and Strother [15] related the SNR in the conventional (or non-TOF) PET image to the square root of the noise equivalent count rate (NECR)

$$\text{SNR} = \sqrt{\text{NECR}} = \text{const} \times n^{-1/2}\left[\frac{T^2}{(T+S+R)}\right]^{1/2} \quad (1)$$

where T, S and R are the true, scatter and random coincidence count rates, respectively, and n is the number of image elements contributing to a projection of the sinogram. In the case of a uniform distribution of activity in a cylindrical of diameter D, and where d is the size of the image element, $n = D/d$. The word "const" relates to the geometry modification and the duration of the acquisition. The expression between the brackets is commonly referred to as NECR, thus, any reference to NECR throughout the rest of this study, would be the same. In the literature, it is assumed that the NECR term for SNR in TOF images is the same as for conventional images. If we assume so, the SNR expressions for TOF and conventional images differ only for the value of n. It should be mentioned that Eq. (1) assumes a uniform distribution of activity in a uniform object and further modification is necessary for other distributions of activity. Since in our study, the SNR gain due to TOF is discussed, the constant in Eq. (1) has no effect on the upcoming results. Thus, SNR improvement has been estimated as proportional to the square root of $D/\Delta x$, where D is the radial dimension of the object to be imaged, and Δx is the spatial uncertainty associated with the CRT of the scanner

$$\text{SNR}_{TOF} \cong \sqrt{D/\Delta x}\,\text{SNR}_{conv} \quad (2)$$

Such gain is higher for systems with better CRT, and for bigger objects. Although Eq. (2) is commonly used to estimate SNR gain due to TOF, since it is assumed that the variance contribution due to true, scatter and random coincidences decrease by the same factor, it is not a realistic approximation [2].

Conti proposed a simple variation of Eq. (2) as a function of random fraction [36]

$$\text{SNR}_{TOF-Conti} \cong \sqrt{\frac{D}{\Delta x}}\sqrt{\frac{T+S+\beta R}{T+S+\beta^2 R}}\,\text{SNR}_{conv} \quad (3)$$

or, in terms of the random fraction $R_f = R/(T+S)$,

$$\text{SNR}_{TOF-Conti} \cong \sqrt{\frac{D}{\Delta x}}\sqrt{\frac{1+\beta R_f}{1+\beta^2 R_f}}\,\text{SNR}_{conv} \quad (4)$$

where $\beta = D/D_{FOV}$ (patient size over scanner FOV diameter). D_{FOV} is defined by the coincidence time window ($D_{FOV} = ct_w/2$).

Since there is a very weak dependence of SNR gain on scatter fraction [37], Eq. (4) corresponds to a more precise estimate of the SNR gain using TOF, and for a given patient size, it is a function of the random fraction. Eq. (4) converges to Eq. (2) at low random fraction values.

For SNR due to TOF calculation, we use Eq. (2), but this time, we do not assume that the NECR term in (1) is the same for TOF and non-TOF. In fact, in this study, we clearly show that NECR terms for TOF and non-TOF images are not the same. As such, TOF
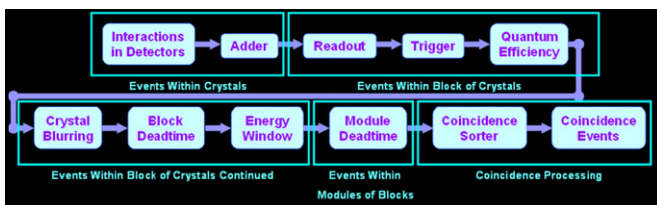
SNR gain is calculated via:

$$\mathrm{SNR}_{TOF}/\mathrm{SNR}_{non\text{-}TOF} \cong \sqrt{D/\Delta x}\sqrt{\frac{\mathrm{NECR}_{TOF}}{\mathrm{NECR}_{non\text{-}TOF}}} \qquad (5)$$

By using the same formula, $\mathrm{NECR}_{non\text{-}TOF}$ and NECR_{TOF} are measured separately in the simulated absence and presence of TOF, respectively. We also compare the TOF SNR gain results of GATE simulation with those achieved through the model proposed by Conti [36], and hypothesize that with increasing random fractions, the measured gain in (5) will also increase, as predicted by the Conti's model.

3. Results

3.1. Overall robustness verification

While the GATE Monte Carlo package has been extensively validated, we performed overall robustness checks for the code for the cases of estimating axial sensitivity (3D), axial and transaxial detection position, gamma non-collinearity angle distribution (deg.) and positron annihilation distance (mm).

Fig. 2 illustrates the simulated axial sensitivity (3D) of the Discovery RX (DRX) scanner. The 3D sensitivity is not uniformly distributed axially and falls off rapidly as one approaches the edges of the axial FOV.

Fig. 3a shows the transaxial detection position which is a 2D histogram of the X and Y coordinates of the annihilation photons in the DRX detector rings. The distribution of detection is completely homogeneous.

The DRX axial detection position is shown in Fig. 3b. It is a 1D histogram of the Z coordinate of detected annihilation photons. It illustrates the behavior of the detectors in axial direction. The histogram drops in inactive areas.

Finally, positron annihilation distance was characterized, as shown in Fig. 4 depicting the number of 18 F positrons as a function of their annihilation distance. Most of the positrons annihilate in distances less than 0.5 mm while a few annihilate in distances more than 1 mm.

3.2. Validation by comparison

The results are compared to published data from Kemp et al. [14] for the sensitivity, scatter fraction and count rates. A comparison of the sensitivity of the GATE simulation to experimental values is presented in Table 1. The third column lists the
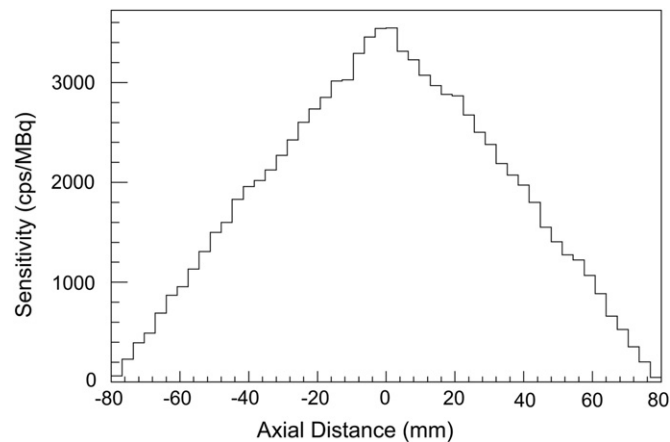
Fig. 3. (a) The DRX transaxial detection position in x–y plane. (b) The DRX axial detection position. The histogram drops in inactive areas.

Fig. 4. Positron annihilation distance for 18 F. The result is in good agreement with experimental value.

results when a 92.5% crystal detection efficiency is applied to individual events within the blocks in the digitizer. This efficiency is set using *setCrystalQE* within the GATE module and represents the efficiency for detection of scintillation photons after they are generated in the crystals (incorporating (i) the fraction of

Fig. 2. The simulated DRX sensitivity as a function of axial position. It is obtained by applying a 5.85 ns timing window and a 425–650 keV energy window.
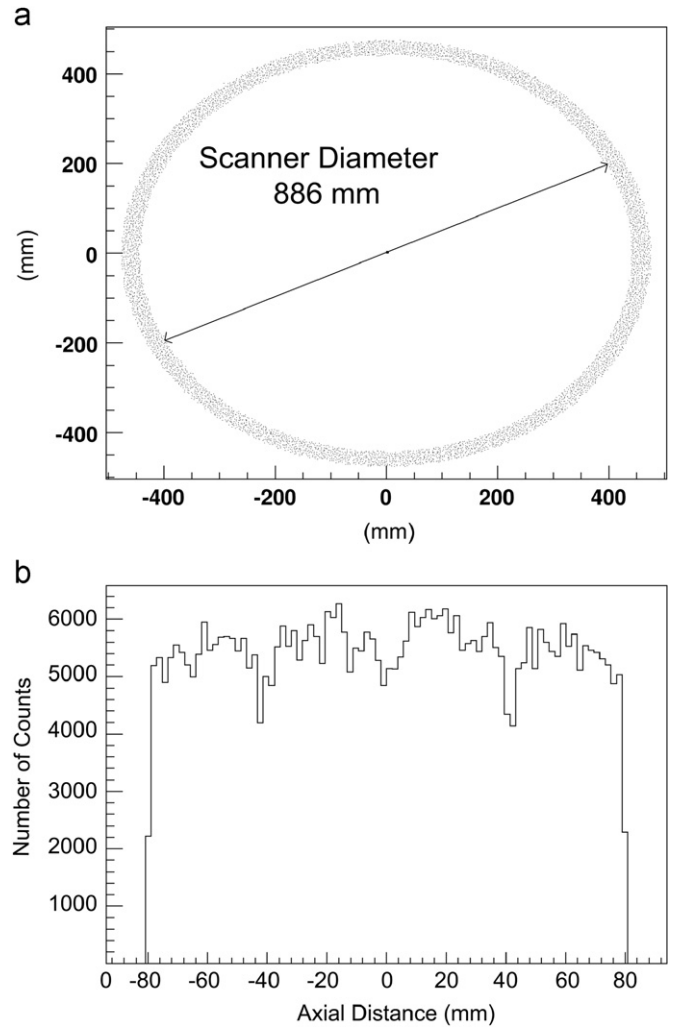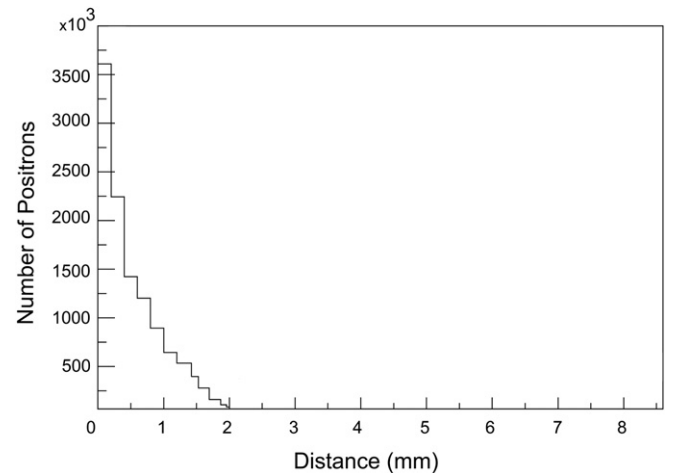
Table 1
Comparison of 3D sensitivity measurements between the GE Discovery RX PET scanner and the GATE simulation with efficiency corrections.

Radial position (cm)	Published data [8] (cps/kBq)	GATE with efficiency corrections (cps/kBq)
R0=0	7.30	7.36
R10=10	7.54	7.55
Ratio R0/R10	0.968	0.974

Table 2
Comparison of 3D scatter fraction measurements between the GE Discovery RX PET scanner and the GATE simulation.

Activity (kBq/ml)	10	15	21.7	22.5
GATE simulation data (%)	33.1	32.1	32.6	32.5
Published data [8] (%)	34.5	36	37.9	38
Relative difference (%)	4	10.8	14	14.5

generated scintillation photons that make it to PMT photo-cathode, and (ii) the efficiency by which the incident light is converted to a detected signal by the PMT). This efficiency was varied as a free parameter until the best agreement with experimental results was obtained. The mentioned QE of 92.5% can satisfactorily match the sensitivity in experimental results.

Table 2, shows a comparison of the scatter fraction results of the GATE simulations to the measured data for different activity concentrations. The simulated scatter fractions are very close to the measured value (within 4–14%). The difference between the two experimental data points for the 425–650 keV energy windows is also about 4%.

The count rate performance for trues, randoms, and noise equivalent counts without randoms subtraction are shown in Figs. 5 and 6 for different time coincidence windows. In Fig. 5, the random event rates were divided by a factor of 5 to enable both rates to be displayed in one place.

The simulated peak true count rate was 465.2 kcps occurring at 32.5 kBq/ml and the simulated peak NECR was 124.1 kcps at 22.8 kBq/ml, respectively, for the measured coincidence window of 6.5 ns.

The experimental peak true count rate of 453.6 kcps at an effective activity concentration of 30.8 kBq/ml were matched by the simulated results to within 2.5% and 5.5%, respectively. The measured count rate curves also resulted in a peak NECR of 117.7 kcps at 21.7 kBq/ml. The peak NECR and the related activity concentration values obtained using the GATE simulations were within 5.4% and 5% of published data, respectively.

3.3. Evaluation of electronic improvement and TOF performance

For various hardware coincidence windows, Figs. 5 and 6 plots the random and true rates and NECR for the NEMA 2001 scatter phantom in a 3-D mode as a function of activity concentrations. The data in these figures have been obtained without utilization of TOF information. It is clearly seen that the randoms rates are increasingly reduced with improving coincidence window widths. It is also seen that true event rates at lower activity concentrations, as expected, were not affected by varying the coincidence window widths. However, at higher activity concentrations, true rates were slightly increased for shorter coincidence windows, attributed to the maximum total event rate of the coincidence processor and limited bandwidth of wires or buffer capacities of the I/O interfaces. In Fig. 6 important improvements are noticeable as assessed via the NECR concept. The peak NECR
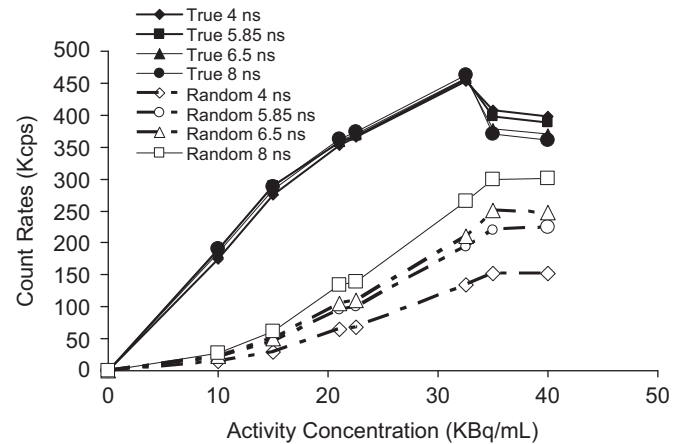

Fig. 5. Random and true rates vs. activity concentration for varying coincidence window width. The object imaged was the NEMA 2001 scatter phantom. The random event rates were divided by a factor of 5 to enable both rates shown in one figure.
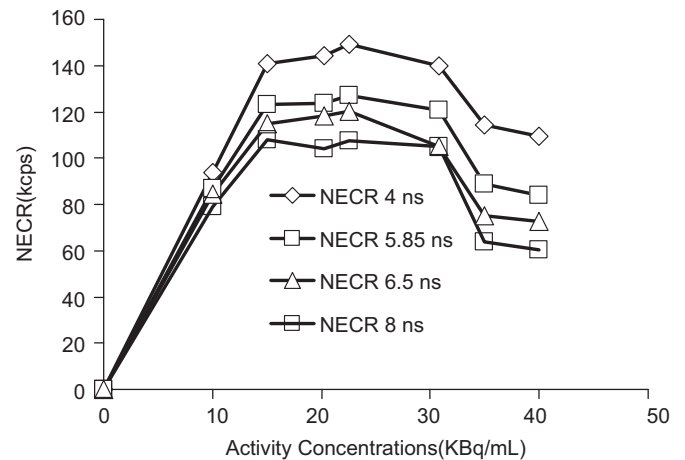

Fig. 6. NECR vs. activity concentration for varying coincidence window width in the non-TOF scanner. The object imaged was the NEMA 2001 scatter phantom.

had increased by ~50% when utilizing the smaller coincidence window width.

For exploring the achievable gains in the scanner performance, the time coincidence window was set with the practically used value in the DRX scanner in clinic, 4 ns, in various activities and CRTs. Fig. 7 shows NECR values as a function of activity concentrations for varying CRTs within the TOF context. These values were obtained for a 4 ns total coincidence window. Also the NECR for a non-TOF scanner was plotted. Major improvements can be realized merely by improving the CRT. The improved NECR performance for CRTs less than 500 ps FWHM is especially noticeable.

A comparison of the TOF SNR gain results of the GATE simulations to those of the Conti's model [36] is reported in Table 3. The values were obtained for different activities and CRTs of 300 and 500 ps FWHM, which seems to be possible with current technology, based on a 4 ns total coincidence window with NEMA 2001 scatter and count rate measurement phantom as the object. As can be observed, the TOF SNR gain increases with increasing random fractions in very good agreement with Conti's model, an effect not predicted by the conventional model. The relative differences were calculated as the percentage difference relative to the mean.

Table 4 summarizes the potential benefits that could be achieved if the CRT in the Discovery RX PET/CT scanner were to

be improved. It should be noted that the calculations in Table 4 are based on a 4 ns total coincidence window with NEMA 2001 scatter and count rate measurement phantom as the object.

4. Discussion

TOF PET was extensively studied in the 1980s and eventually discarded, as other performance tradeoffs imposed by the CsF and BaF scintillator then used for TOF PET outweighed the advantages. The new scintillators (e.g. LYSO) have the potential to give the advantages of TOF without the disadvantages. The Discovery RX PET/CT scanner uses LYSO scintillators yet because of the electronics, TOF remains to be implemented in this scanner. Because the potential performance improvements offered by TOF PET are substantial, in this study, we performed Monte Carlo simulations to explore achievable gains in PET performance when the CRT is improved.

In Fig. 2, the increase in 3D sensitivity is due to the increase in the effective geometrical solid angle covered by the scanner. In 3D mode, as the increase in the number of LORs depends on the number of crystal rings, there is a much stronger variation in sensitivity, which peaks in the center of the axial FOV.
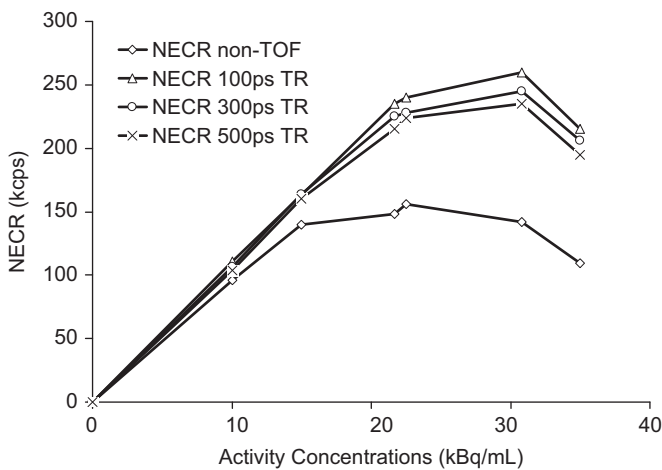

Fig. 7. NECR vs. activity concentration for varying coincidence resolving times. The values were obtained for a 4 ns coincidence window.

The homogeneity of the distribution in Fig. 3a shows the isotropic radiations besides the uniformity of detection. Behavior of the detectors in axial direction is shown in Fig. 3b. As a matter of fact, the DRX has 4 modules of crystals in the axial direction and therefore 3 layers of packing material has been used between them, thus no counts should be detected in those inactive areas. However, due to the scatter and the LOR mispositioning, the axial position of the corresponding LORs is improperly histogrammed in those areas. It should be noted that the weighted average positioning in the block is the main cause of LOR mispositioning.

The distribution of 18F positron annihilation distances is shown in the Fig. 4. The distribution obtained is cusp-shaped with long tails rather than Gaussian shaped, which is in good agreement with published measure data by Sánchez-Crespo et al. [38]. The simulated positron range distribution has a maximum value at the zero distance and 0.3 mm FWHM in comparison with the measured 0.19 mm FWHM for soft tissues [38].

As Fig. 7 clearly shows, the NECR curve for TOF is not the same as for non-TOF. Thus, the traditional approximation of SNR improvement due to TOF is not realistic and Eq. (2) is an underestimation of the actual SNR gain we can actually achieve with TOF. From the data reported in Table 3, SNR TOF gain increases with the random fraction and improved CRT, in a perfect agreement with the modified traditional estimate for SNR gain which accounts the effect of randoms in TOF PET. In higher activities, the relative difference increase between the results of the GATE simulation and the Conti's model is attributed to the saturation of randoms due to an overflow of a memory buffer and/or limited

Table 4
Predicted benefits as a function of coincidence resolving time in LYSO-based Discovery RX PET/CT scanner when using 4 ns coincidence window.

Coincidence resolving time	Performance gain
500 ps FWHM	Factor of 2.2–2.3 reduction in random rates Factor of 1.48 increase in NECR Factor of 2–2.1 improvement in SNR
300 ps FWHM	Factor of 2.6 reduction in random rates Factor of 1.6 increase in NECR. Factor of 2.7–2.9 improvement in SNR
100 ps FWHM	Factor of 2.7 reduction in random rates. Factor of 1.75 increase in NECR. Factor of 3.5 improvement in SNR

Table 3
TOF SNR gains as the results of GATE simulations and proposed model by Conti. The values were obtained for a 4 ns coincidence window. The relative difference is calculated as the percentage difference relative to the mean.

Activity (kBq/ml)	$T+S$ (kcps)	Random fraction (R_f)	Coincidence resolving time (FWHM) (ps)	TOF SNR gain		
				GATE simulation Eq. (5)	**Conti's model [26] Eq. (4)**	**Relative difference (%)**
10	281	0.25	300	2.36	2.18	7.9
			500	1.82	1.69	7.4
15	414	0.35	300	2.38	2.20	7.9
			500	1.82	1.71	6.2
21.7	555	0.58	300	2.73	2.25	19.3
			500	2.09	1.74	18.3
22.5	564	0.6	300	2.75	2.25	20
			500	2.11	1.75	18.7
30.8	734	0.92	300	2.86	2.3	21.7
			500	2.17	1.79	19.2
35	692	1.09	300	2.92	2.34	22.1
			500	2.18	1.82	18

bandwidth of wires or buffer capacities of the I/O interfaces that decrease the role of randoms in the model. Also, Conti's model is not fully validated for different phantoms and activities, and as our Monte Carlo based simulation results include each particles' trajectory and arrival time, we can expect better TOF SNR gains than those achieved by the Conti's analytical model in higher activities.

If the CRT in Discovery RX PET/CT scanner can be improved, significant improvements can be realized which are summarized in Table 4. For example, with CRTs of 500 ps FWHM, deemed possible with current technology, a factor of 2.3 reduction in random rates, factor of 1.5 increase in NECR and factor of 2.1 improvement in SNR are achievable. In other words, the results of this study show that in addition to the present high sensitivity of Discovery RX PET/CT scanner, the implementation of TOF with proper CRT can efficiently further improve the image quality statistics in this scanner (Table 4).

5. Conclusion

The development of fast scintillator such as LSO and LYSO has already provided PET cameras with improved performance characteristics. However, the excellent timing properties have not yet been fully exploited in PET. If the CRT in Discovery RX PET/CT scanner can be improved, the implementation of TOF with proper CRT can efficiently improve the image quality in this scanner. It appears that the investigation of TOF PET should prove very fruitful for the particular scanner studied in this work, and more generally, for a large range of PET scanners using the new technology. Having successfully simulated the DRX scanner and utilization of TOF information, our research goal is to use the Monte Carlo simulation technique to arrive at powerful, accurate and feasible reconstruction algorithms.

Acknowledgment

References

[1] D.L. Snyder, D.G. Politte, IEEE Trans. Nucl. Sci. NS30 (3) (1983) 1843.
[2] W.W. Moses, IEEE Trans. Nucl. Med. 50 (2003) 1325.
[3] A. Rahmim, H. Zaidi, Nucl. Med. Commun. 29 (2008) 193.
[4] R. Allemand, C. Gresset, J. Vacher, J. Nucl. Med. 21 (153-1) (1980) 55.
[5] N.A. Mullani, J. Markham, M.M. Ter-Pogossian, J. Nucl. Med. 21 (1980) 1095.
[6] M.M. Ter-Pogossian, N.A. Mullani, D.C. Ficke, J. Markham, D.L. Snyder, J. Compiti. Assist. Tomogr. 5 (1981) 227.
[7] T. Kimble, M. Chou, B.H.T Chai, Scintillation properties of LYSO crystals, IEEE Nuclear Science Symposium and Medical Imaging Conference Record, Norfolk, 2002, vol. 3, pp. 1434.
[8] C. Lois, B.W. Jakoby, M.J. Long, K.F. Hubner, et al., J. Nucl. Med. 51 (2010) 237.
[9] D.J. Kadrmas, M.E. Casey, M. Conti, B.W. Jakoby, C. Lois, D.W. Townsend, J. Nucl. Med. 50 (2009) 1315.
[10] S. Surti, A Kuhn, M.E. Werner, A.E. Perkins, J. Kolthammer, J.S. Karp, J. Nucl. Med. 48 (2007) 471.
[11] G El Fakhri, S. Surti, C.M. Trott, J. Scheuermann, J.S. Karp, J. Nucl. Med. 52 (2011) 11.
[12] G. Muehllehner, J.S. Karp, Phys. Med. Biol. 51 (2006) 117.
[13] M.E. Daube-Witherspoon, S. Surti, A. Perkins, C.C.M. Kyba, et al., Phys. Med. Biol. 55 (2010) 45.
[14] B.J. Kemp, C. Kim, J.J. Williams, A. Ganin, V.J. Lowe, J. Nucl. Med. 47 (12) (2006) 1960.
[15] S.C. Strother, M.E. Casey, E.J. Hoffman, IEEE Trans. Nucl. Sci. NS37 (2) (1990) 783.
[16] M. Dahlbom, C. Schiepers, J. Czernin, IEEE Trans. Nucl. Sci. 52 (5) (2005) 1386.
[17] S. Pajevic, M.E. Daube-Witherspoon, S.L. Bacharach, RE. Carson, IEEE Trans. Med. Imaging 17 (1998) 9.
[18] R.D. Badawi, P.K. Marsden, B.F. Cronin, J.L. Sutcliffe, M.N. Maisey, Phys. Med. Biol. 41 (1996) 1755.
[19] D. Brasse, P.E. Kinahan, C. Lartizien, C. Comtat, M. Casey, C. Michel, J. Nucl. Med. 46 (5) (2005) 859.
[20] H. Watabe, K. Matsumoto, M. Senda, H. Iida, Ann. Nucl. Med. 20 (2006) 189.
[21] P. Geramifar, M.R. Ay, M. Shamsaei Zafarghandi, G. Loudos, A. Rahmim, Iran. J. Nucl. Med. 17 (2) (2009) 26.
[22] D. Strulab, G. Santin, D. Lazaro, V. Breton, C. Morel, J. Nucl. Phys. 125 (2003) 75.
[23] S. Jan, D. Benoit, E. Becheva, T. Carlier, F. Cassol, et al., Phys. Med. Biol. 56 (2011) 881.
[24] I. Buvat, D. Lazaro, J. Nucl. Instr. and Meth. Phys. 569 (2006) 323.
[25] A. Rahmim, K. Dinelle, J.C. Cheng, et al., IEEE Trans. Med. Imag. 27 (2008) 1018.
[26] A. Rahmim, J.C. Cheng, K. Dinelle, et al., J. Nucl. Med. Commun. 29 (2008) 574.
[27] S. Jan, C. Comtat, D. Strul, G. Santin, R. Trebossen, IEEE Trans. Nucl. Med. 52 (2005) 627.
[28] J. Tang, A. Rahmim, R. Lautamaki, M.A. Lodge, F.M. Bengel, B.M.W. Tsui, Phys. Med. Biol. 54 (2009) 3161.
[29] OpenGATE Collaboration, GATE Users Guide, Version 1.0.0, May 2004, ⟨www-lphe.epfl.ch/GATE/⟩.
[30] "NEMA standards publication NU 2-2001: Performance measurements of positron emission tomographs," Technical report (National Electrical Manufactures Association, Washington, DC, 2001).
[31] D.R. Schaart, S. Seifert, R. Vinke, H.T. van Dam, P. Dendooven, H. Löhner, F.J. Beekman, Phys. Med. Biol. 55 (2010) 179.
[32] M. Conti, L. Eriksson, H. Rothfuss, C.L. Melcher, IEEE Trans. Nucl. Sci. NS56 (3) (2009) 926.
[33] K. Chang Lyong, G.Ch. Wang, S. Dolinsky, IEEE Trans. Nucl. Sci. NS56 (5) (2009) 2580.
[34] C.C.M. Kyba, J. Glodo, E.V.D van Loef, J.S. Karp, K.S. Shah, IEEE Trans. Nucl. Sci. NS55 (2008) 1404.
[35] G.L. Brownell, J.A. Correia, R.G. Zamenhof, Positron instrumentation, Recent Advances in Nuclear Medicine, vol. 5, Grune and Stratton, New York, 1978.
[36] M. Conti., IEEE Trans. Nucl. Sci. NS53 (3) (2006) 1188.
[37] J.A. Kimdom, J. Qi, W.W. Moses, Effect of random and scatter fractions in variance reduction using time-of-flight information, IEEE Nuclear Science Symposium Conference Record, 2003, vol. 4, pp. 2571.
[38] A. Sanchez-Crespo, P. Andreo, S.A. Larsson, Eur. J. Nucl. Med. Mol. Imaging 31 (2004) 44.